actuators

MDPI

Article

Polymorphic Phase Transition and Piezoelectric Performance of $BaTiO_3$-$CaSnO_3$ Solid Solutions

Qian Wang [1], Hong-Ze Yan [1], Xian Zhao [1,2] and Chun-Ming Wang [1,2,*]

[1] School of Physics, State Key Laboratory of Crystal Materials, Shandong University, Jinan 250100, China; wangq_sdu@sdu.edu.cn (Q.W.); yanhz@mail.sdu.edu.cn (H.-Z.Y.); zhaoxian@sdu.edu.cn (X.Z.)

[2] Center for Optics Research and Engineering (CORE), Key Laboratory of Laser and Infrared System of Ministry of Education, Shandong University, Qingdao 266237, China

* Correspondence: wangcm@sdu.edu.cn

Abstract: $BaTiO_3$-based piezoelectric ceramics have attracted considerable attention in recent years due to their tunable phase structures and good piezoelectric properties. In this work, the $(1-x)BaTiO_3$_$xCaSnO_3$ ($0.00 \leq x \leq 0.16$, abbreviated as BT_xCS) solid solutions, were prepared by traditional solid-state reaction methods. The phase transitions, microstructure, dielectric, piezoelectric, and ferroelectric properties of BT-xCS have been investigated in detail. The coexistence of rhombohedral, orthorhombic, and tetragonal phases near room temperature, i.e., polymorphic phase transition (PPT), has been confirmed by X-ray diffraction and temperature-dependent dielectric measurements in the compositions range of $0.06 \leq x \leq 0.10$. The multiphase coexistence near room temperature provides more spontaneous polarization vectors and facilitates the process of polarization rotation and extension by an external electric field, which is conducive to the enhancement of piezoelectric response. Remarkably, the composition of BT-0.08CS exhibits optimized piezoelectric properties with a piezoelectric coefficient d_{33} of 620 pC/N, electromechanical coupling factors k_p of 58%, k_t of 40%, and a piezoelectric strain coefficient d_{33}* of 950 pm/V.

Keywords: barium titanate ($BaTiO_3$); piezoelectric properties; polymorphic phase transition

Citation: Wang, Q.; Yan, H.-Z.; Zhao, X.; Wang, C.-M. Polymorphic Phase Transition and Piezoelectric Performance of $BaTiO_3$-$CaSnO_3$ Solid Solutions. *Actuators* **2021**, *10*, 129. https://doi.org/10.3390/act10060129

Academic Editor: Kenji Uchino

Received: 4 April 2021
Accepted: 4 June 2021
Published: 13 June 2021

1. Introduction

In recent years, $BaTiO_3$-based piezoelectric ceramics have attracted considerable attention because of their tunable phase structures and good piezoelectric response [1–10]. Generally, the boosted piezoelectric response is always accompanied with the formation of morphotropic phase boundary (MPB) or polymorphic phase transition (PPT). The enhanced piezoelectric properties near MPB are associated with easy path for polarization rotation as revealed in anisotropic flattened free energy profiles [11–15]; and the mechanisms of the increased piezoelectric properties near PPT are related to the lower energy barriers of multiphase coexistence, as the composition-induced phase transitions at PPT can facilitate the process of polarization rotation and extension under an external electric field, leading to enhanced dielectric and piezoelectric properties [16–22]. Therefore, the vital point of improving piezoelectric response of $BaTiO_3$ is to induce the phase transitions by forming MPB or PPT via composition designing strategy [23–30].

The schematic diagrams of phase transitions of pure $BaTiO_3$ in the temperature range from −90 °C to 130 °C are shown in Figure 1. There are four phases: rhombohedral (*R*) phase, orthorhombic (*O*) phase, tetragonal (*T*) phase, and cubic (*C*) phase; and three phase transitions: ferroelectric-ferroelectric phase transitions of *R* to *O* phase with $T_{R\text{-}O}$ of ~−90 °C and *O* to *T* phase with $T_{O\text{-}T}$ of ~5 °C, and the ferroelectric-paraelectric phase transition *T* to *C* phase with $T_{R\text{-}O}$ of ~130 °C. Great efforts have been made to adjust phase transitions of $BaTiO_3$-based ceramics in order to enhance their dielectric, ferroelectric, and piezoelectric properties. For example, the strontium-doped $BaTiO_3$ ceramics exhibit diffused phase transitions due to compositional inhomogeneity [31–33]; the $BaTiO_3$-BiMO_3

(where *M* represents Sc^{3+}, In^{3+}, etc.) solid solutions present phase transition from normal ferroelectrics to relaxor ferroelectrics by compositional design, and the hysteresis loop characteristics of relaxor ferroelectrics are conducive to the enhancement of energy storage properties [34–36]; the (Ba, Ca)$(Ti_{1-x}M_x)O_3$ (where *M* represents Zr^{4+}, Hf^{4+}, Sn^{4+}, etc.) ceramics are the most widely investigated $BaTiO_3$-based ceramics with enhanced piezoelectric properties in recent years due to their tunable phase transitions with the variation of *M* concentration [37–43]. A high piezoelectric constant d_{33} of 485 pC/N with electromechanical coupling coefficient k_p of 39% and mechanical quality factor Q_m of 191 was achieved in the $(Ba_{0.95}Ca_{0.05})(Ti_{0.90}Sn_{0.10})O_3$ ceramics with 3 mol% Li_2CO_3 by constructing the phase coexistence of *R* and *T* phases at room temperature (RT) [37]. The improved piezoelectric and dielectric properties, with a d_{33} of 407 pC/N, dielectric constant ε_r of 5500, and dielectric loss tanδ of 0.3%, have been obtained in the $(1-x)Ba_{0.98}Ca_{0.02}Ti_{0.94}Sn_{0.06}O_3$-$xBa_{0.85}Ca_{0.15}Ti_{0.9}Zr_{0.1}O_3$ ceramics, where the phase coexistence of orthorhombic and tetragonal phases is identified with x = 0.40 [38]. Significantly enhanced piezoelectric properties with a d_{33} of 515 pC/N and a field-induced strain d_{33}* of 1293 pm/V at 10 kV were acquired in the ternary system $BaTiO_3$-$CaTiO_3$-$BaSnO_3$, where the several phase transitions (*R*-*O*, *O*-*T* and *T*-*C*) are designed near RT [39]. As indicated in previous investigations, (Ba, Ca)$(Ti_{1-x}M_x)O_3$ based ceramics are good piezoelectric ceramic materials operating at room temperature. Therefore, the investigations on the enhanced piezoelectric properties of (Ba, Ca)$(Ti_{1-x}M_x)O_3$ solid solutions are of great interest for $BaTiO_3$-based ceramics.

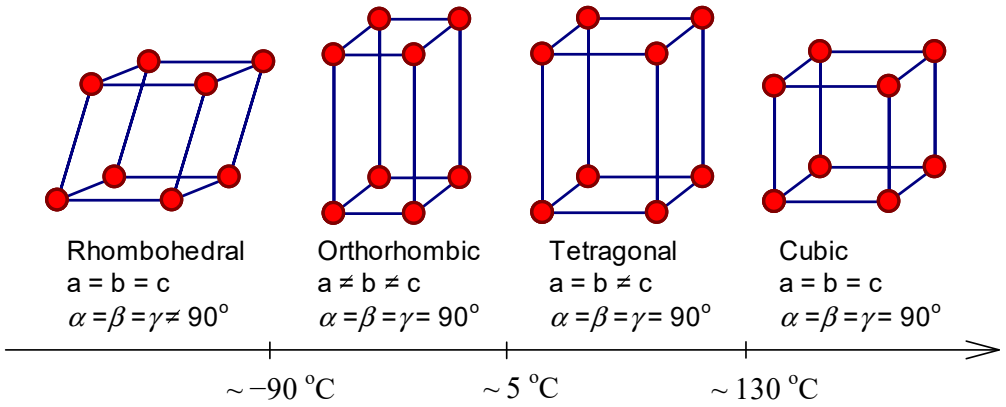

Figure 1. Schematic diagrams of phase transitions for pure $BaTiO_3$ in the temperature range from −90 °C to 130 °C.

Note that the *B*-site doping cations of Zr^{4+}, Hf^{4+}, Sn^{4+} have similar effects on inducing the phase transitions in the (Ba, Ca)$(Ti_{1-x}M_x)O_3$ ceramics, while the Sn^{4+} ion has a significant impact on the construction of phase boundary [41]. Additionally, it has been confirmed that the introduction of $CaSnO_3$ decreases the c/a ratio of $BaTiO_3$ [44], and the distortion of lattice structure may have great influence on the piezoelectric properties. However, few reports on the dielectric, piezoelectric, and ferroelectric properties of the $CaSnO_3$ modified $BaTiO_3$ ceramics exist in the literature. Therefore in this work, $(1-x)BaTiO_3$-$xCaSnO_3$ (BT-*x*CS) solid solutions have been prepared by the conventional solid-state reaction method. The microstructure, phase structure, dielectric, ferroelectric, and piezoelectric properties have been investigated in detail.

2. Materials and Methods

$(1-x)BaTiO_3$-$xCaSnO_3$ (abbreviated as BT-*x*CS, x = 0.00, 0.02, 0.04, 0.06, 0.08, 0.10, 0.12, 0.14, and 0.16) ceramics were prepared by conventional solid-state reaction method. Analytical-grade $BaCO_3$ (>99.5%), TiO_2 (>99.8%), $CaCO_3$ (>99.5%), and SnO_2 (>99.5%) were used as raw materials. The powders were weighed according to the stoichiometric compositions, and then wet-milled in polyethylene bottles with ZrO_2 balls for 12 h in ethanol. The milled powders were dried and calcined at 1200 °C for 3 h. Afterwards, the calcined powders were milled, dried, grinded, and granulated with polyvinyl alcohol (PVA)

binder and subsequently pressed into discs with diameters of 12.0 mm and thicknesses of 2.0 mm at a pressure of 150 MPa. After binder burn-out at 650 °C, the green compacts were placed in Al_2O_3 crucibles with self-source. The samples were sintered at 1380 °C for 3 h, and then furnace-cooled down to room temperature.

The phase structure was characterized by an X-ray diffractometer (Smartlab SE, Rigaku Corporation, Tokyo, Japan) with Cu K_α radiation in the 2θ range of 20–80°. The natural surface morphology of the sintered ceramics was carried out by field-emission scanning electron microscopy (Helios G4 UC, Thermo Fisher Scientific, Hillsboro, OR, USA), and the intercept method was used to measure the grain size using the software of ImageJ. Before the electrical measurements, both sides of the sintered ceramics were polished, and fired at 600 °C for 30 min after the silver electrodes were screen-printed on both polished surfaces of ceramics. The dielectric properties were tested by an impedance analyzer (E4990A, Keisight Technologies, Santa Rosa, CA, USA). Hysteresis loops were measured by a ferroelectric analyzer (TF Analyzer 2000, aixACCT Systems GmbH, Aachen, Germany). The piezoelectric constant d_{33} was measured using a d_{33} meter (YE2730A, Sinocera Piezotronics, Inc., Yangzhou, China) after the sample was poled in silicone oil under a direct-current (DC) electric field of 40 kV/cm at room temperature. The electromechanical coupling factor k_t and k_p were determined by the IEEE resonance method with E4990A impedance analyzer.

3. Results and Discussion

3.1. Phase Structure

Figure 2a presents the powder X-ray diffraction (PXRD) patterns of BT-xCS ($0.00 \leq x \leq 0.16$) ceramics, and the standard diffraction peaks are also presented for comparison, as indicated in the bottom of Figure 2a with vertical black lines. Herein the JCPDS cards of Nos. 85–1790, 81–2200, 79–2265 and 79–2263 are rhombohedral, orthorhombic, tetragonal, and cubic phase of BT, respectively. As shown in Figure 2a, all the BT-xCS compositions exhibit pure perovskite structure without any trace of secondary or impure phases detected. In terms of Shannon's work, the effective ionic radius of $^{XII}Ba^{2+}$, $^{VI}Ti^{4+}$, $^{XII}Ca^{2+}$, and $^{VI}Sn^{4+}$ are 161 pm, 60.5 pm, 134 pm, and 69 pm, respectively. According to the fundamentals of radius matching rule, Ca^{2+} ions and Sn^{4+} ions occupy the *A*-site (Ba-site) and *B*-site (Ti-site) of $BaTiO_3$ lattice, respectively. Additionally, the tolerance factor of perovskite structure is usually used to evaluate the stability of crystal structure, which can be determined by the following equation:

$$t = (R_A + R_O)/\sqrt{2}(R_B + R_O) \quad (1)$$

where R_A, R_B, and R_O represent the ionic radius of the *A*-, *B*-site, and O^{2-} in ABO_3 structure, respectively. It is commonly recognized that the perovskite structure is stable with $0.77 < t < 1.09$, and the value of t locates between 1.062 and 1.039 for BT-xCS ($0.00 \leq x \leq 0.16$), indicating the stable structure of BT-xCS solid solutions in this work. The enlarged (200) diffraction peaks with angles from 44.6° to 47.0° are given in Figure 2b to clearly show the phase evolutions. It is clear that the diffraction peaks of the compositions with $x < 0.04$ are assigned to the *T* phase, and those of the compositions with $x > 0.12$ correspond to the *C* phase. Note that the diffraction peaks of the compositions with $0.06 \leq x \leq 0.10$ are not separately matched well with those four *R*, *T*, *O*, and *C* phases, which can be described as phase coexistence. Similar results have been reported in other elements modified BT-based ceramics [38–42]. Furthermore, the (200) peak shifts slightly towards higher degrees with the increase of x content, indicating the shrinkage of the lattice parameters, and this can be ascribed to the decrease of the ionic radius in *A*-site, 134 pm for Ca^{2+} compared with 161 pm for Ba^{2+} in 12-fold coordination.

3.2. Dielectric Properties

In order to further investigate the phase transition behavior of BT-xCS ceramics, the temperature-dependent dielectric constant ε_r and dielectric loss tanδ measured at 100 kHz in the temperature range from −50 °C to 150 °C are shown in Figure 3. The room

temperature dielectric constant ε_r and dielectric loss tanδ of BT-xCS measured at 100 kHz are listed in Table 1. The value of ε_r increases initially from 1966 to 10,811 as the x content increases from 0.00 to 0.14, and then decreases to 8,803 at x = 0.16. Meanwhile, the dielectric loss tanδ of BT-xCS ceramics is low (tanδ < 0.06) within the investigated temperature range. The variation of ε_r is mainly due to the evolution of phase transitions around room temperature. As shown in Figure 3, there are two significant dielectric anomalies for the compositions of x = 0.00 and 0.02 within the investigated temperature range, and the dielectric anomalies correspond to the ferroelectric-ferroelectric phase transition (*O*-*T*) at $T_{O\text{-}T}$ and the paraelectric-ferroelectric phase transition (*T*-C) at T_C, respectively. For the compositions of $0.04 \leq x \leq 0.10$, another ferroelectric-ferroelectric phase transition (*R*-*O*) at $T_{R\text{-}O}$ arises. With the increase of x content, the $T_{R\text{-}O}$ and $T_{O\text{-}T}$ shift to higher temperature, while the T_C shifts to lower temperature, resulting in the merging of three phase transition peaks into one broad peak at T_C for the composition of x = 0.12, and the *R*-*O* and *O*-*T* phase transitions disappear gradually with $x \geq 0.12$. The phase transition temperatures ($T_{R\text{-}O}$, $T_{O\text{-}T}$, and T_C) of BT-xCS are also summarized in Table 1. The $T_{R\text{-}O}$ increases from −26.1 °C to 5.2 °C as the x content increases from 0.04 to 0.10, the $T_{O\text{-}T}$ increases from 16.6 °C to 24.5 °C as the x increases from 0.00 to 0.10, and the T_C decreases from 126.9 °C to −4.3 °C as the x increases from 0.00 to 0.16, respectively.

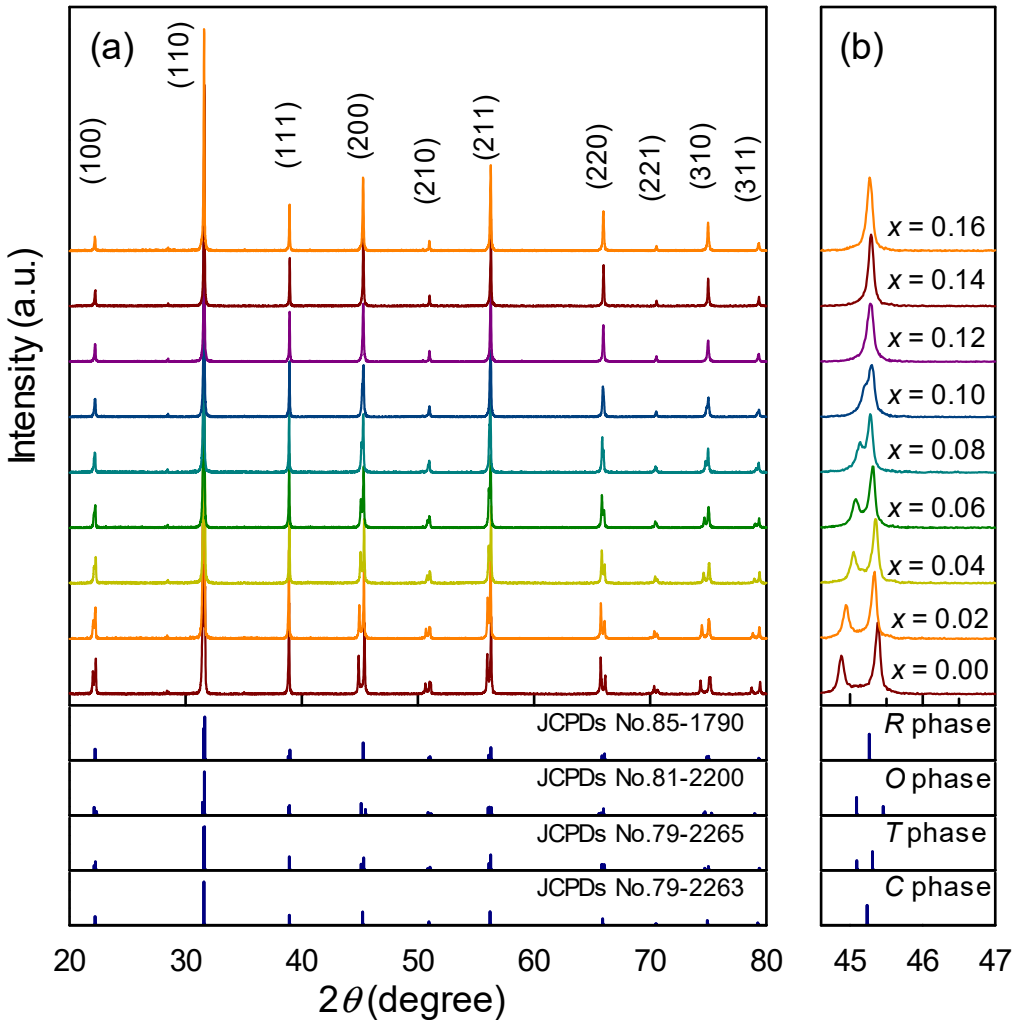

Figure 2. (**a**) Powder X-ray diffraction patterns of BT-xCS in the 2θ range of 20–80°, and (**b**) the enlarged patterns from 44.6° to 47.0°.

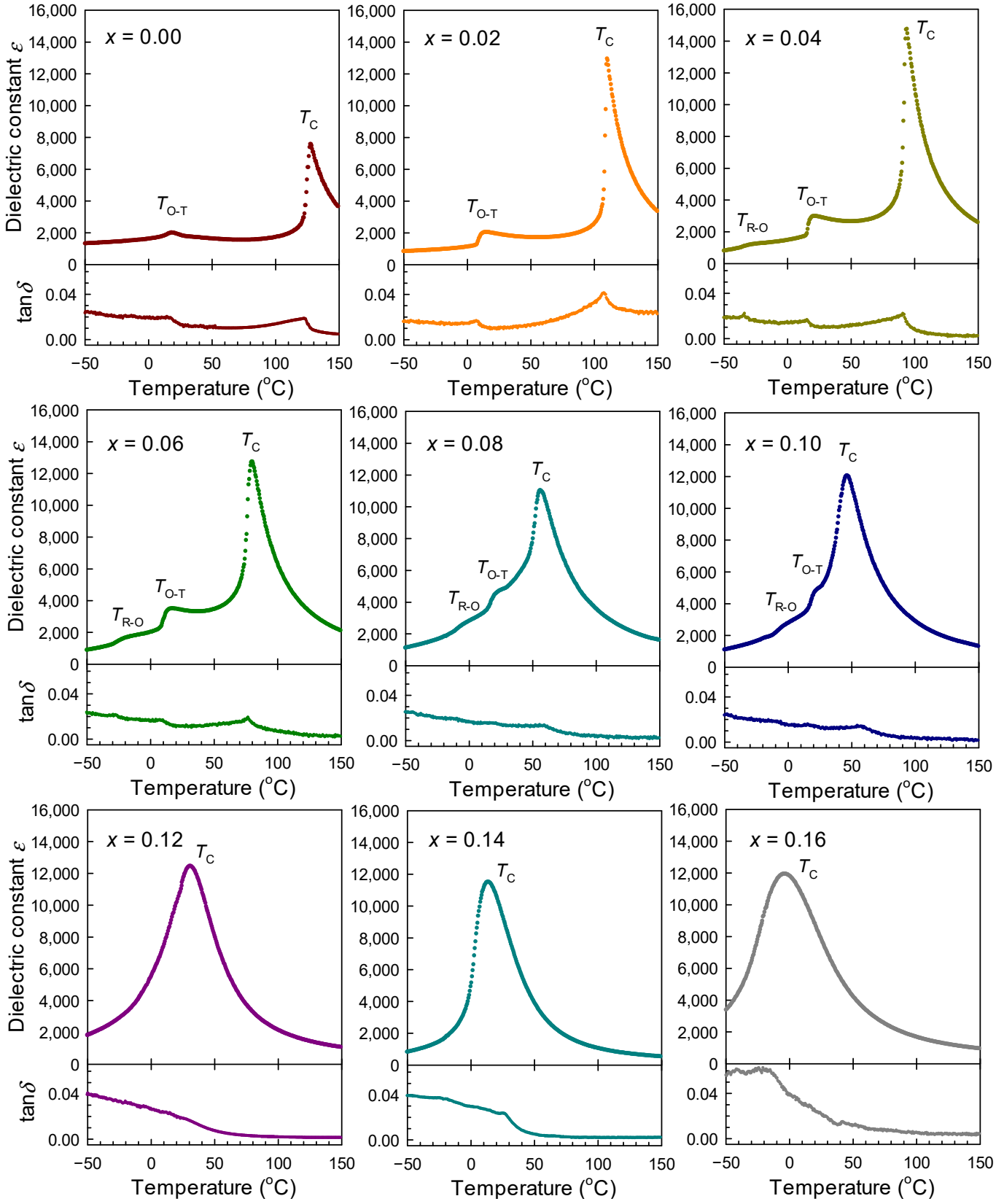

Figure 3. Temperature-dependent dielectric constant ε and loss tanδ of BT-xCS ($0.00 < x < 0.16$) measured at 100 kHz.

Table 1. Dielectric properties and phase transition temperatures of BT-*x*CS.

x	ε_r *	tanδ (%) *	$T_{R\text{-}O}$ (°C)	$T_{O\text{-}T}$ (°C)	T_C (°C)
0.00	1966	1.23	-	16.6	126.9
0.02	1979	0.97	-	15.4	110.3
0.04	2955	1.15	−26.1	17.9	93.6
0.06	3462	1.18	−12.9	18.2	79.6
0.08	4410	1.32	−1.7	19.9	52.4
0.10	4809	1.37	5.2	24.5	42.5
0.12	10,091	2.02	-	-	28.6
0.14	10,811	2.36	-	-	12.5
0.16	8803	2.43	-	-	−4.3

* Data measured at 100 kHz and at room temperature.

3.3. Phase Transition

The phase diagrams of BT-*x*CS are established according to the temperature-dependent dielectric results, as shown in Figure 4a. The phase diagrams consist of three ferroelectric phase regions, *R*, *O*, and *T* phases and one paraelectric phase region, *C* phase, which visually demonstrates the phase transitions. The T_C decreases almost linearly with the increase of x content, which is mainly influenced by the substitution of Sn^{4+} for Ti^{4+} ions, as the Ca^{2+} in *A*-site of BT generally has little effects on the T_C [45]. However, the substitution of Sn^{4+} for Ti^{4+} significantly affects the stability of BO_6 octahedron and decreases the tetragonality c/a. Similar results have been reported in Sn^{4+}-modified $BaTiO_3$ [46,47]. The $T_{R\text{-}O}$ and $T_{O\text{-}T}$ increase at different rising rate as the x content increases from 0.00 to 0.10, and merge into T_C around room temperature for the composition of x = 0.12. Herein the shadow area represents the phase components around room temperature. Figure 4b presents the lattice parameters as a function of x content based on the refining PXRD data. The composition-dependent lattice parameters are considered as the further evidence of phase evolution. As indicated by the yellow symbols (lattice parameters of *T* phase), the c decreases but the a increases as the x content increases from 0.00 to 0.10, which means that the ratio of c/a decreases and also suggests that the structure tends to be an *R* or *C* phase. Furthermore, combining the PXRD results, the phase structure for the compositions of $0.06 \leq x \leq 0.10$ cannot be simply identified as the *T* phase, and thereby the lattice parameters of these compositions are also given based on the *R* and *O* phases. As shown in Figure 4a,b, the results of lattice parameters show close conformance with the dielectric phase diagrams. The $T_{O\text{-}T}$, $T_{R\text{-}O}$, and T_C coincide gradually at room temperature for the compositions of $0.06 \leq x \leq 0.10$, resulting in the formation of polymorphic phase transition (PPT) of *R*-*O* and *O*-*T* phase transitions around room temperature, i.e., the coexistence of *R*, *O*, and *T* phases.

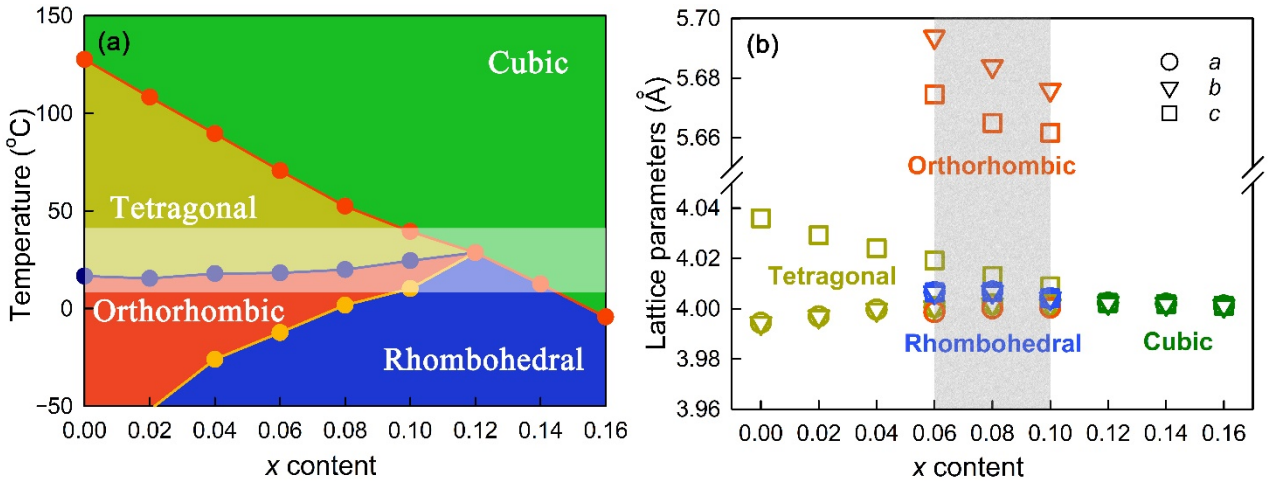

Figure 4. (**a**) Phase diagrams, and (**b**) lattice parameters as a function of CS content.

3.4. Microstructural Properties

Previous investigations have shown that the $BaTiO_3$-based ceramics exhibit an enhanced dielectric response as the grain size decreases to micron level due to the grain size effect [48,49]. The SEM images and grain distributions of BT-xCS ($0.02 \leq x \leq 0.16$) ceramics are shown in Figure 5. All the samples are densely sintered with distinctive grain boundaries, and the relative density of each composition is over 95%. The insets of Figure 5 are the distributions of grain size and the average grain size corresponding to each composition. It is obvious that the microstructure of BT-xCS is dependent on the substitution of CS. The grain distributions are inhomogeneous in the compositions of $x < 0.06$, which are similar to the grain morphology of pure BT [36]. For example, the grain size of large grains in the composition of $x = 0.02$ is approximately 20 μm and that of small grains is only about 4 μm. The variation of grain growth in the range of $0.06 \leq x \leq 0.10$ may be ascribed to the phase transition around room temperature induced by composition. With further increase of x content, the grain tends to distribute homogeneously and the grain size is nearly unchanged in the compositions of $x > 0.08$. However, further doping of CS ($x = 0.16$) leads to the decrease in grain size, which may be attributed to the excess doping of CS concentrates near grain boundaries and inhibits the grain growth of BT-xCS ceramics.

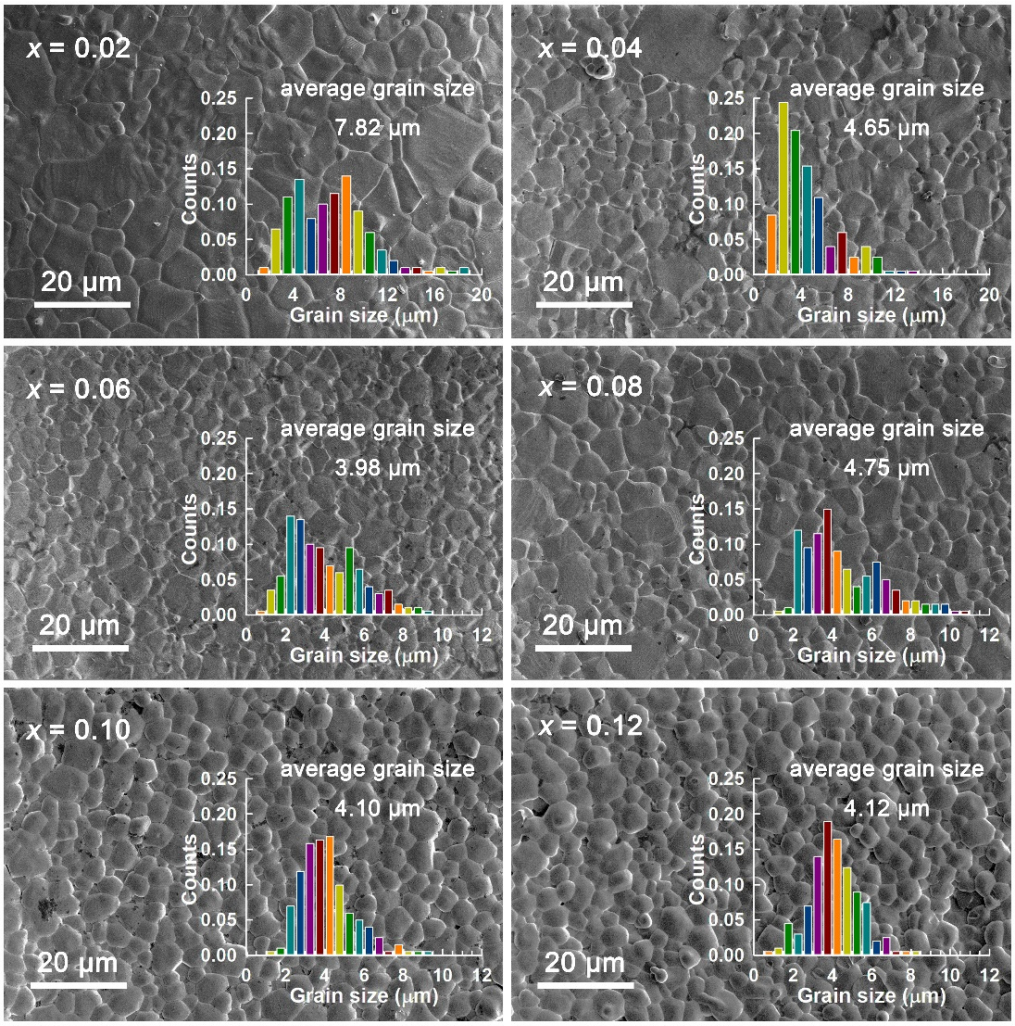

Figure 5. *Cont.*

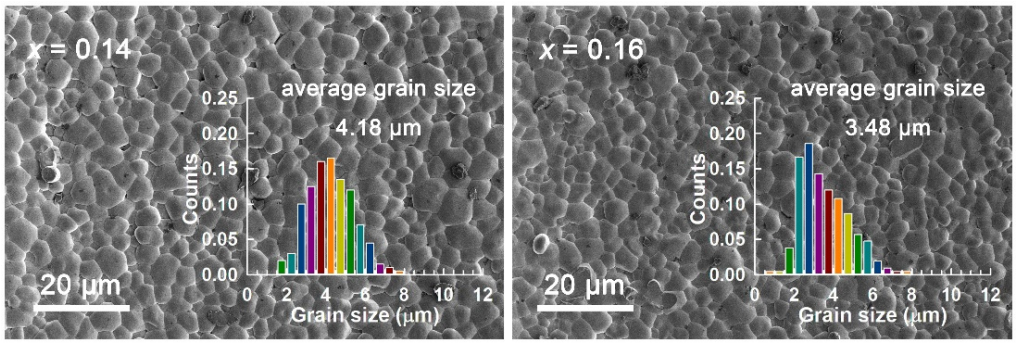

Figure 5. SEM images of BT-*x*CS and the corresponding grain size distributions.

3.5. Piezoelectric Properties

Figure 6 shows the composition-dependent piezoelectric constant d_{33}, planar electromechanical coupling factor k_p, and thickness electromechanical coupling factor k_t of BT-*x*CS ceramics. The d_{33} values are summarized in Table 2; the values of d_{33} increases initially from 350 pC/N for pure $BaTiO_3$ to 620 pC/N for the composition of $x = 0.08$, and then decreases rapidly to 130 pC/N at $x = 0.16$. There are two reasons for the enhancement of piezoelectric response. According to the polarization deflection theory proposed by Fu and Cohen [18], the coexistence of *R*, *O*, *T* phases at $x = 0.08$ provides more spontaneous polarization vectors [41,42,50], resulting in the increase of piezoelectricity. On the other hand, the low energy barriers in the region of phase boundaries can greatly facilitate the process of polarization rotation and extension under an external electric field [16–18], which can be responsible for the significant enhancement of piezoelectric response. Meanwhile, there are similar variation tendencies of k_p and k_t, and the values of k_p and k_t increase initially as the *x* content increases from 0.00 to 0.08, and then decreases with the *x* content further increasing to 0.16. The composition with $x = 0.08$ exhibits optimal piezoelectric properties, with the maximum d_{33} value of 620 pC/N, k_p of 58%, and k_t of 40%.

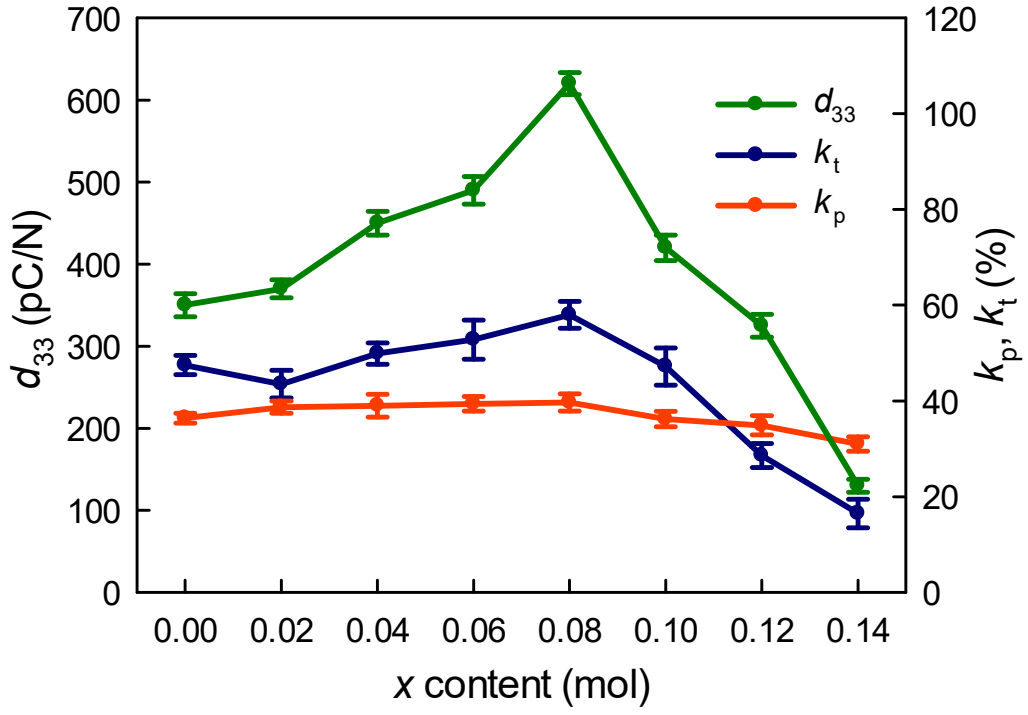

Figure 6. Composition-dependent piezoelectric constant d_{33}, planar electromechanical coupling factor k_p, and thickness electromechanical coupling factor k_t of BT-*x*CS ceramics.

Table 2. Ferroelectric and piezoelectric properties of BT-*x*CS ceramics.

x	P_m (μC/cm^2)	P_r (μC/cm^2)	E_C (kV/cm)	d_{33}(pC/N)	d_{33}*(pm/V)
0.00	25.4	11.40	2.57	352	525
0.02	24.8	10.39	2.61	374	598
0.04	23.8	8.92	2.17	450	629
0.06	22.0	6.99	1.77	491	799
0.08	20.3	5.74	1.36	620	950
0.10	17.8	2.55	0.97	420	633
0.12	16.1	1.29	0.68	325	414
0.14	15.2	0.68	0.58	130	265
0.16	13.2	0.29	0.57	-	210

3.6. Ferroelectric Properties

Figure 7a shows the polarization-electric field (*P*-*E*) loops of BT-*x*CS ($0.04 \leq x \leq 0.16$) under the driven electric field of 40 kV/cm. The *P*-*E* loops tend to become "slim" with the increase of x content. The loop for the composition of $x = 0.16$ presents a "curve", demonstrating that the BT-0.16CS ceramic is transformed to the paraelectric phase [51]. The maximum polarization P_m, remnant polarization P_r and coercive field E_c, derived from *P*-*E* loops, are displayed in Figure 7b as a function of x content, and the corresponding values are summarized in Table 2. It is clear that the P_m, P_r, and E_c exhibit the similar decline tendency with the increase of x content. Note that the value of E_c decreases from 2.57 kV/cm to 0.57 kV/cm as the x content increases from 0.00 to 0.16, leading to an easier domain switching under the external electric field. The reduction of E_c can be attributed to the instability of the ferroelectric domains. It has been well established that the stability of ferroelectric domain is determined by the coupling of *A*-site cations and BO_6 octahedron with ferroelectric properties for an ABO_3 type perovskite structure, and the distortion of lattice structure induced by the substitution of Ca^{2+} and Sn^{4+} weakens the coupling between *A*-site cation and BO_6 octahedron of BT-*x*CS, resulting in the instability of the ferroelectric domains and thereby decreasing the value of E_c [52,53]. Meanwhile, P_m and P_r decrease from 25.4 μC/cm^2 and 11.40 μC/cm^2 to 13.2 μC/cm^2 and 0.29 μC/cm^2 as the x content increases from 0.00 to 0.16, respectively. Figure 7c exhibits the bipolar field-induced strain as a function of electric field of BT-*x*CS ($0.04 \leq x \leq 0.16$) ceramics under the electric field of 40 kV/cm. Butterfly-shape *S*-*E* loops are observed in the compositions of $x < 0.10$, and this type loop is intrinsically determined by their ferroelectric phase structure. The loops tend to be slender in the compositions of $x > 0.10$. The values of positive strain S_{pos} and negative strains S_{neg} increase initially to 4.02% and 0.75% at $x = 0.08$, and then decrease to 0.67% and almost zero at $x = 0.16$, respectively. Since the external electric field is much higher than E_c, the values of S_{pos} are very close to that of the maximum strain induced by the unipolar electric field (S_{uni}) [54]. The unipolar field-induced strain of BT-0.08CS is presented in Figure 7d, and the maximum value of S_{uni} reaches 0.38% under the electric field of 40 kV/cm. The derived piezoelectric strain coefficient d_{33}* as a function of x content is shown in the inset of Figure 7d. The values of d_{33}* are calculated according to the following equation:

$$d_{33}^* = S_{max}/E_{max} \quad (2)$$

where S_{max} and E_{max} are the maximum values of strain and electric field obtained from the unipolar strain loops, as d_{33}* calculated from unipolar *S*-*E* loops are more representable than that from bipolar loops [45]. As shown in Table 2, the excellent piezoelectric response with large d_{33}* value of 950 pm/V is obtained for the BT-0.08CS, which is caused by the PPT around the room temperature [39].

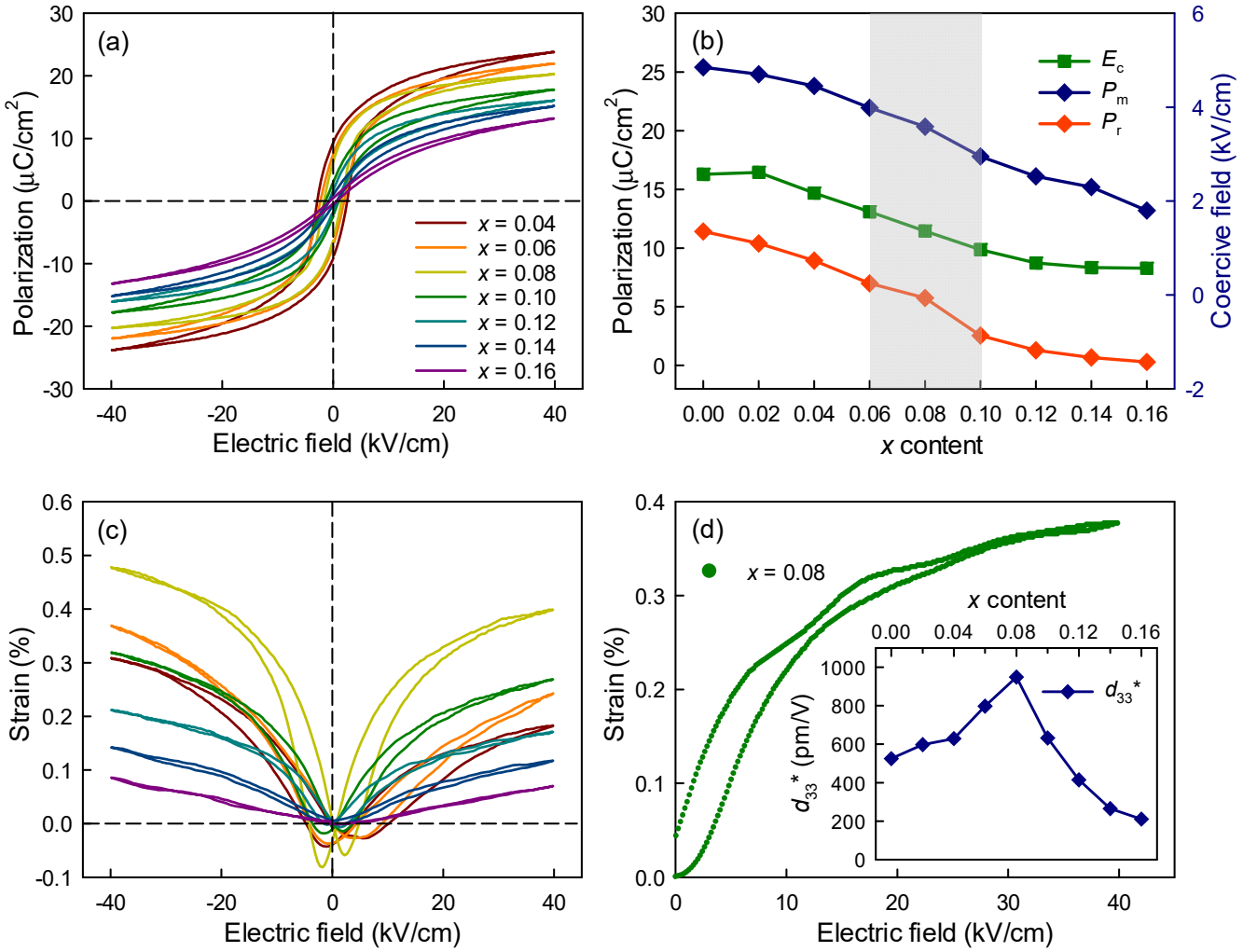

Figure 7. (**a**) *P*-*E* loops of BT-*x*CS, (**b**) the corresponding coercive field E_c, the maximum polarization P_m, and the remnant polarization P_r as a function of CS contents, (**c**) the bipolar *S*-*E* loops of BT-*x*CS, and (**d**) the unipolar *S*-*E* loop of BT-0.08CS as a function of applied electric field.

4. Conclusions

The $(1 - x)BaTiO_3$-$xCaSnO_3$ ($0.00 \leq x \leq 0.16$) solid solutions have been prepared by the traditional solid-state reaction methods. The coexistence of *R*, *O*, *T* phases in the compositions with $0.06 \leq x \leq 0.10$ is revealed by the PXRD results, and also confirmed by the temperature-dependent dielectric measurements. The composition of BT-0.08CS exhibits optimized piezoelectric properties, which is attributed to the polymorphic phase transition. A high piezoelectric coefficient d_{33} of 620 pC/N and a large piezoelectric strain coefficient d_{33}* of 950 pm/V are achieved, demonstrating the enhanced piezoelectric properties of BT-*x*CS ceramics.

Author Contributions: Conceptualization, C.-M.W.; investigation, Q.W. and H.-Z.Y.; writing—original draft preparation, Q.W.; writing—review and editing, Q.W., X.Z., and C.-M.W.; supervision, C.-M.W.; funding acquisition, X.Z. and C.-M.W.; All authors have read and agreed to the published version of the manuscript.

Funding: This research was funded by the National Natural Science Foundation of China under Grant No. 51872166, the Key Research and Development Program of Shandong Province of China under Grant No. 2019GGX102064, the Key Research and Development Program of Shandong Province of China under Grant No. 2019JZZY010313, and Shandong Provincial Natural Science Foundation-Quantum Science Research Joint fund under Grant No. ZR2020LLZ006.

Data Availability Statement: Please contact with the corresponding author.

Conflicts of Interest: The authors declare no conflict of interest. The funders had no role in the design of the study; in the collection, analyses, or interpretation of data; in the writing of the manuscript, or in the decision to publish the results.

References

1. Shrout, T.R.; Zhang, S.J. Lead-free piezoelectric ceramics: Alternatives for PZT? *J. Electroceram.* **2007**, *19*, 113–126. [CrossRef]
2. Rödel, J.; Jo, W.; Seifert, K.T.P.; Anton, E.-M.; Granzow, T.; Damjanovic, D. Perspective on the Development of Lead-free Piezoceramics. *J. Am. Ceram. Soc.* **2009**, *92*, 1153–1177. [CrossRef]
3. Li, W.; Xu, Z.; Chu, R.; Fu, P.; Zang, G. Enhanced ferroelectric properties in $(Ba_{1-x}Ca_x)(Ti_{0.94}Sn_{0.06})O_3$ lead-free ceramics. *J. Eur. Ceram. Soc.* **2012**, *32*, 517–520. [CrossRef]
4. Wu, B.; Xiao, D.; Wu, W.; Zhu, J.; Chen, Q.; Wu, J. Microstructure and electrical properties of $(Ba_{0.98}Ca_{0.02})(Ti_{0.94}Sn_{0.06})O_3$-modified $Bi_{0.51}Na_{0.50}TiO_3$ lead-free ceramics. *Ceram. Int.* **2012**, *38*, 5677–5681. [CrossRef]
5. Panda, P.K. Review: Environmental friendly lead-free piezoelectric materials. *J. Mater. Sci.* **2009**, *44*, 5049–5062. [CrossRef]
6. Takenaka, T.; Maruyama, K.-I.; Sakata, K. $(Bi_{1/2}Na_{1/2})TiO_3$-$BaTiO_3$ System for Lead-Free Piezoelectric Ceramics. *Jpn. J. Appl. Phys.* **1991**, *30*, 2236–2239. [CrossRef]
7. Liu, W.; Ren, X. Large Piezoelectric Effect in Pb-Free Ceramics. *Phys. Rev. Lett.* **2009**, *103*, 257602. [CrossRef]
8. Horchidan, N.; Padurariu, L.; Ciomaga, C.E.; Curecheriu, L.; Airimioaei, M.; Doroftei, F.; Tufescu, F.; Mitoseriu, L. Room temperature phase superposition as origin of enhanced functional properties in $BaTiO_3$-based ceramics. *J. Eur. Ceram. Soc.* **2020**, *40*, 1258–1268. [CrossRef]
9. Tan, Y.; Viola, G.; Koval, V.; Yu, C.; Mahajan, A.; Zhang, J.; Zhang, H.; Zhou, X.; Tarakina, N.V.; Yan, H. On the origin of grain size effects in $Ba(Ti_{0.96}Sn_{0.04})O_3$ perovskite ceramics. *J. Eur. Ceram. Soc.* **2019**, *39*, 2064–2075. [CrossRef]
10. Pomyai, P.; Munthala, D.; Sonklin, T.; Supruangnet, R.; Nakajima, H.; Janphuang, P.; Dale, S.M.; Glaum, J.; Pojprapai, S. Electrical fatigue behavior of $Ba_{0.85}Ca_{0.15}Zr_{0.1}Ti_{0.9}O_3$ ceramics under different oxygen concentrations. *J. Eur. Ceram. Soc.* **2021**, *41*, 2497–2505. [CrossRef]
11. Ahart, M.; Somayazulu, M.; Cohen, R.E.; Ganesh, P.; Dera, P.; Mao, H.-K.; Hemley, R.J.; Ren, Y.; Liermann, P.; Wu, Z. Origin of morphotropic phase boundaries in ferroelectrics. *Nature* **2008**, *451*, 545–548. [CrossRef]
12. Kutnjak, Z.; Petzelt, J.; Blinc, R. The giant electromechanical response in ferroelectric relaxors as a critical phenomenon. *Nature* **2006**, *441*, 956–959. [CrossRef] [PubMed]
13. Gao, J.; Xue, D.; Wang, Y.; Wang, D.; Zhang, L.; Wu, H.; Guo, S.; Bao, H.; Zhou, C.; Liu, W.; et al. Microstructure basis for strong piezoelectricity in Pb-free $Ba(Zr_{0.2}Ti_{0.8})O_3$-$(Ba_{0.7}Ca_{0.3})TiO_3$ ceramics. *Appl. Phys. Lett.* **2011**, *99*, 092901. [CrossRef]
14. Gao, J.; Zhang, L.; Xue, D.; Kimoto, T.; Song, M.; Zhong, L.; Ren, X. Symmetry determination on Pb-free piezoceramic $0.5Ba(Zr_{0.2}Ti_{0.8})O_3$-$0.5(Ba_{0.7}Ca_{0.3})TiO_3$ using convergent beam electron diffraction method. *J. Appl. Phys.* **2014**, *115*, 054108. [CrossRef]
15. Xue, D.; Zhou, Y.; Bao, H.; Zhou, C.; Gao, J.; Ren, X. Elastic, piezoelectric, and dielectric properties of $Ba(Zr_{0.2}Ti_{0.8})O_3$-$50(Ba_{0.7}Ca_{0.3})TiO_3$ Pb-free ceramic at the morphotropic phase boundary. *J. Appl. Phys.* **2011**, *109*, 054110. [CrossRef]
16. Damjanovic, D. A morphotropic phase boundary system based on polarization rotation and polarization extension. *Appl. Phys. Lett.* **2010**, *97*, 062906. [CrossRef]
17. Zhou, C.; Liu, W.; Xue, D.; Ren, X.; Bao, H.; Gao, J.; Zhang, L. Triple-point-type morphotropic phase boundary based large piezoelectric Pb-free material-$Ba(Ti_{0.8}Hf_{0.2})O_3$-$(Ba_{0.7}Ca_{0.3})TiO_3$. *Appl. Phys. Lett.* **2012**, *100*, 222910. [CrossRef]
18. Fu, H.; Cohen, R.E. Polarization rotation mechanism for ultrahigh electromechanical response in single-crystal piezoelectrics. *Nature* **2000**, *403*, 281–283. [CrossRef]
19. Zhang, L.; Zhang, M.; Wang, L.; Zhou, C.; Zhang, Z.; Yao, Y.; Zhang, L.; Xue, D.; Lou, X.; Ren, X. Phase transitions and the piezoelectricity around morphotropic phase boundary in $Ba(Zr_{0.2}Ti_{0.8})O_3$-$x(Ba_{0.7}Ca_{0.3})TiO_3$ lead-free solid solution. *Appl. Phys. Lett.* **2014**, *105*, 162908. [CrossRef]
20. Zhao, L.; Ke, X.; Zhou, Z.; Liao, X.; Li, J.; Wang, Y.; Wu, M.; Li, T.; Bai, Y.; Ren, X. Large electrocaloric effect over a wide temperature range in $BaTiO_3$-modified lead-free ceramics. *J. Mater. Chem. C* **2019**, *7*, 1353–1358. [CrossRef]
21. Gao, J.; Ke, X.; Acosta, M.; Glaum, J.; Ren, X. High piezoelectricity by multiphase coexisting point: Barium titanate derivatives. *MRS Bull.* **2018**, *43*, 595–599. [CrossRef]
22. Guo, H.; Voas, B.K.; Zhang, S.; Zhou, C.; Ren, X.; Beckman, S.P.; Tan, X. Polarization alignment, phase transition, and piezoelectricity development in polycrystalline $0.5Ba(Zr_{0.2}Ti_{0.8})O_3$-$0.5(Ba_{0.7}Ca_{0.3})TiO_3$. *Phys. Rev. B* **2014**, *90*, 014103. [CrossRef]
23. Xue, D.; Zhou, Y.; Bao, H.; Gao, J.; Zhou, C.; Ren, X. Large piezoelectric effect in Pb-free $Ba(Ti,Sn)O_3$-$x(Ba,Ca)TiO_3$ ceramics. *Appl. Phys. Lett.* **2011**, *99*, 122901. [CrossRef]
24. Zhou, P.-F.; Zhang, B.-P.; Zhao, L.; Zhao, X.-K.; Zhu, L.-F.; Cheng, L.-Q.; Li, J.-F. High piezoelectricity due to multiphase coexistence in low-temperature sintered $(Ba,Ca)(Ti,Sn)O_3$-CuO*x* ceramics. *Appl. Phys. Lett.* **2013**, *103*, 172904. [CrossRef]
25. Zhu, L.-F.; Zhang, B.-P.; Zhao, X.-K.; Zhao, L.; Yao, F.-Z.; Han, X.; Zhou, P.-F.; Li, J.-F. Phase transition and high piezoelectricity in $(Ba,Ca)(Ti_{1-x}Sn_x)O_3$ lead-free ceramics. *Appl. Phys. Lett.* **2013**, *103*, 072905. [CrossRef]
26. Chen, Z.; Li, Z.; Ma, M.; Zhao, T.; Qiu, J.; Ding, J. Effect of Nd_2O_3 doping on the electrical properties of $Ba_{0.96}Ca_{0.04}Ti_{0.90}Sn_{0.10}O_3$ ceramics. *J. Rare Earths* **2018**, *36*, 745–749. [CrossRef]

27. Zhao, L.; Zhang, B.-P.; Wang, W.-Y.; Ding, Y.-H.; Zhang, S.-M.; Zhu, L.-F.; Wang, N. Effect of B_2O_3 on phase structure and electrical properties of CuO-modified (Ba,Ca)(Ti,Sn)O_3 lead-free piezoceramics sintered at a low-temperature. *Ceram. Int.* **2016**, *42*, 7366–7372. [CrossRef]
28. Zhao, L.; Zhang, B.-P.; Zhou, P.-F.; Zhu, L.-F.; Wang, N. Piezoelectric and ferroelectric properties of (Ba,Ca)(Ti,Sn)O_3 lead-free ceramics sintered with Li_2O additives: Analysis of point defects and phase structures. *Ceram. Int.* **2016**, *42*, 1086–1093. [CrossRef]
29. Noritake, K.; Sakamoto, W.; Yuitoo, I.; Takeuchi, T.; Hayashi, K.; Yogo, T. Fabrication of lead-free piezoelectric Li_2CO_3-added (Ba,Ca)(Ti,Sn)O_3 ceramics under controlled low oxygen partial pressure and their properties. *Jpn. J. Appl. Phys.* **2017**, *57*, 021501. [CrossRef]
30. Chen, Z.-H.; Li, Z.-W.; Xu, J.-J.; Guo, H.-F.; Zhang, B.; Ding, J.-N.; Qiu, J.-H. Improvement on electrical properties of $Ba_{0.9}Ca_{0.1}Ti_{0.9}Sn_{0.1}O_3$ ceramics with the addition of CeO_2. *J. Alloys Compd.* **2017**, *720*, 562–566. [CrossRef]
31. Tiwari, V.S.; Singh, N.; Pandey, D. Diffuse ferroelectric transition and relaxational dipolar freezing in (Ba,Sr)TiO_3. *J. Phys. Condens. Matter* **1995**, *7*, 1441–1460. [CrossRef]
32. Singh, N.; Pandey, D. Diffuse ferroelectric transition and relaxational dipolar freezing in: II. Role of Sr concentration in the dynamics of freezing. *J. Phys. Condens. Matter* **1996**, *8*, 4269–4287. [CrossRef]
33. Singh, N.; Singh, A.P.; Prasad, C.D.; Pandey, D. Diffuse ferroelectric transition and relaxational dipolar freezing in: III. Role of order parameter fluctuations. *J. Phys. Condens. Matter* **1996**, *8*, 7813–7827. [CrossRef]
34. Ogihara, H.; Randall, C.A.; Trolier-McKinstry, S. Weakly Coupled Relaxor Behavior of $BaTiO_3$-$BiScO_3$ Ceramics. *J. Am. Ceram. Soc.* **2009**, *92*, 110–118. [CrossRef]
35. Shen, Z.; Wang, X.; Luo, B.; Li, L. $BaTiO_3$-$BiYbO_3$ perovskite materials for energy storage applications. *J. Mater. Chem. A* **2015**, *3*, 18146–18153. [CrossRef]
36. Wang, Q.; Gong, P.-M.; Wang, C.-M. High recoverable energy storage density and large energy efficiency simultaneously achieved in $BaTiO_3$-Bi($Zn_{1/2}Zr_{1/2}$)O_3 relaxor ferroelectrics. *Ceram. Int.* **2020**, *46*, 22452–22459. [CrossRef]
37. Zhao, L.; Zhang, B.-P.; Zhou, P.-F.; Zhao, X.-K.; Zhu, L.-F. Phase Structure and Property Evaluation of (Ba,Ca)(Ti,Sn)O_3 Sintered with Li_2CO_3 Addition at Low Temperature. *J. Am. Ceram. Soc.* **2014**, *97*, 2164–2169. [CrossRef]
38. Wu, J.; Habibul, A.; Cheng, X.; Wang, X.; Zhang, B. Orthorhombic-tetragonal phase coexistence and piezoelectric behavior in (1-x)(Ba,Ca)(Ti,Sn)O_3-x(Ba,Ca)(Ti,Zr)O_3 lead-free ceramics. *Mater. Res. Bull.* **2013**, *48*, 4411–4414. [CrossRef]
39. Janbua, W.; Bongkarn, T.; Kolodiazhnyi, T.; Vittayakorn, N. High piezoelectric response and polymorphic phase region in the lead-free piezoelectric $BaTiO_3$-$CaTiO_3$-$BaSnO_3$ ternary system. *RSC Adv.* **2017**, *7*, 30166–30176. [CrossRef]
40. Zhu, L.-F.; Zhang, B.-P.; Zhao, X.-K.; Zhao, L.; Zhou, P.-F.; Li, J.-F. Enhanced Piezoelectric Properties of ($Ba_{1-x}Ca_x$)($Ti_{0.92}Sn_{0.08}$)O_3 Lead-Free Ceramics. *J. Am. Ceram. Soc.* **2013**, *96*, 241–245. [CrossRef]
41. Zhao, C.; Wang, H.; Xiong, J.; Wu, J. Composition-driven phase boundary and electrical properties in ($Ba_{0.94}Ca_{0.06}$)($Ti_{1-x}M_x$)O_3 (M = Sn, Hf, Zr) lead-free ceramics. *Dalton Trans.* **2016**, *45*, 6466–6480. [CrossRef] [PubMed]
42. Kalyani, A.K.; Krishnan, H.; Sen, A.; Senyshyn, A.; Ranjan, R. Polarization switching and high piezoelectric response in Sn-modified $BaTiO_3$. *Phys. Rev. B* **2015**, *91*, 024101. [CrossRef]
43. Gao, J.; Hu, X.; Zhang, L.; Li, F.; Zhang, L.; Wang, Y.; Hao, Y.; Zhong, L.; Ren, X. Major contributor to the large piezoelectric response in (1-x)Ba($Zr_{0.2}Ti_{0.8}$)O_3-x($Ba_{0.7}Ca_{0.3}$)TiO_3 ceramics: Domain wall motion. *Appl. Phys. Lett.* **2014**, *104*, 252909. [CrossRef]
44. Donohue, J.; Miller, S.J.; Cline, R.F. The effect of various substituents on the lattice constants of tetragonal titanate. *Acta Cryst.* **1958**, *11*, 693–695. [CrossRef]
45. Acosta, M.; Novak, N.; Rojas, V.; Patel, S.; Vaish, R.; Koruza, J.; Rossetti, G.A.; Rödel, J. $BaTiO_3$-based piezoelectrics: Fundamentals, current status, and perspectives. *Appl. Phys. Rev.* **2017**, *4*, 041305. [CrossRef]
46. Lei, C.; Bokov, A.A.; Ye, Z.G. Ferroelectric to relaxor crossover and dielectric phase diagram in the $BaTiO_3$-$BaSnO_3$ system. *J. Appl. Phys.* **2007**, *101*, 084105. [CrossRef]
47. Du, F.; Cui, B.; Cheng, H.; Niu, R.; Chang, Z. Synthesis, characterization, and dielectric properties of Ba($Ti_{1-x}Sn_x$)O_3 nanopowders and ceramics. *Mater. Res. Bull.* **2009**, *44*, 1930–1934. [CrossRef]
48. Frey, M.H.; Payne, D.A. Grain-size effect on structure and phase transformations for barium titanate. *Phys. Rev. B* **1996**, *54*, 3158–3168. [CrossRef]
49. Chen, Y.; Ye, H.; Wang, X.; Li, Y.; Yao, X. Grain size effects on the electric and mechanical properties of submicro $BaTiO_3$ ceramics. *J. Eur. Ceram. Soc.* **2020**, *40*, 391–400. [CrossRef]
50. Zhu, L.-F.; Zhang, B.-P.; Zhao, L.; Li, S.; Zhou, Y.; Shi, X.-C.; Wang, N. Large piezoelectric effect of (Ba,Ca)TiO_3-xBa(Sn,Ti)O_3 lead-free ceramics. *J. Eur. Ceram. Soc.* **2016**, *36*, 1017–1024. [CrossRef]
51. Long, P.; Liu, X.; Long, X.; Yi, Z. Dielectric relaxation, impedance spectra, piezoelectric properties of (Ba, Ca)(Ti, Sn)O_3 ceramics and their multilayer piezoelectric actuators. *J. Alloys Compd.* **2017**, *706*, 234–243. [CrossRef]
52. Thomas, N.W. A new framework for understanding relaxor ferroelectrics. *J. Phys. Chem. Solids* **1990**, *51*, 1419–1431. [CrossRef]
53. Chen, M.; Xu, Q.; Kim, B.H.; Ahn, B.K.; Chen, W. Effect of CeO_2 addition on structure and electrical properties of $(Na_{0.5}Bi_{0.5})_{0.93}Ba_{0.07}TiO_3$ ceramics prepared by citric method. *Mater. Res. Bull.* **2008**, *43*, 1420–1430. [CrossRef]
54. Zhang, M.-H.; Wang, K.; Zhou, J.-S.; Zhou, J.-J.; Chu, X.; Lv, X.; Wu, J.; Li, J.-F. Thermally stable piezoelectric properties of (K, Na)NbO_3-based lead-free perovskite with rhombohedral-tetragonal coexisting phase. *Acta Mater.* **2017**, *122*, 344–351. [CrossRef]